Biodistribution and radiation dosimetry for the tau tracer ^{18}F-THK-5351 in healthy human subjects

Ing-Tsung Hsiao[1–3*], Kun-Ju Lin[1,2,3*], Kuo-Lun Huang[4], Chin-Chang Huang[4], Han-Shiuan Chen[2], Shiaw-Pyng Wey[1,2], Tzu-Chen Yen[1,2,3], Nobuyuki Okamura[5,6†], Jung-Lung Hsu[4,7†]

[1] Department of Nuclear Medicine and Center for Advanced Molecular Imaging and Translation, Chang Gung Memorial Hospital, Taoyuan, Taiwan

[2] Healthy Aging Research Center and Medical Imaging and Radiological Sciences, Chang Gung University, Taoyuan, Taiwan

[3] Neuroscience Research Center, Chang Gung Memorial Hospital, Taoyuan, Taiwan.

[4] Department of Neurology, Chang Gung Memorial Hospital and Chang Gung University, Taoyuan, Taiwan,

[5] Division of Neuro-imaging, Institute of Development, Aging and Cancer, Tohoku University, Sendai, Japan.

[6] Department of Pharmacology, Faculty of Medicine, Tohoku Medical and Pharmaceutical University, Sendai, Japan.

[7] Graduate Institute of Humanities in Medicine, Taipei Medical University, Taipei, Taiwan.

1

*These authors contributed equally to this work.

†**Corresponding author**: Jung-Lung Hsu, MD, PhD

Department of Neurology, Chang Gung Memorial Hospital and Chang Gung
  University, No. 5, Fuxing St., Guishan Dist., Taoyuan City 333, Taiwan

E-mail: tulu@ms36.hinet.net

†**Co-Corresponding author**: Nobuyuki Okamura, MD, PhD

Department of Pharmacology, Faculty of Medicine, Tohoku Medical and
  Pharmaceutical University, Sendai, Japan

E-mail: nookamura@tohoku-mpu.ac.jp

First author information: Ing-Tsung Hsiao, PhD

Healthy Aging Research Center and Medical Imaging and Radiological Sciences,
Chang Gung University, Taoyuan, Taiwan, No.259, Wenhua 1st Rd., Guishan
Dist., Taoyuan City 333, Taiwan

E-mail: lp97ing@gmail.com

Word count: 4491

Running title: Radiation dosimetry for ^{18}F-THK-5351

Abstract

^{18}F-THK-5351 is a novel radiotracer that demonstrates high binding selectivity and affinity for tau pathology and exhibits better pharmacokinetics in the living brain than previous THK tau probes. The aim of the present study was to estimate the radiation dose of ^{18}F-THK-5351 in humans and to compare the clinical radiation dosimetry results to estimations published previously with preclinical data.

Methods: Serial whole-body positron emission tomography/computed tomography (PET/CT) imaging was performed for 240 min on 12 healthy volunteers after injecting ^{18}F-THK-5351 (mean administered activity: 377.8 ± 14.0 MBq, range: 340–397 MBq). The bladder and gallbladder were delineated on PET images, while the other organs were delineated on CT images. Voided urine activity was recorded. The decay-corrected and normalized ^{18}F-THK-5351 activity of 15 source organ regions as a function of time was entered into the OLINDA/EXM software to calculate the effective dose for each subject following the medical internal radiation dosimetry schema.

Results: Overall, the ^{18}F-THK-5351 injection was well tolerated. The highest mean initial uptakes at 10 min post-injection were measured in the liver (11.4 ± 2.0%), lung (5.7 ± 2.1%), intestine (3.4 ± 0.8%), and kidney (1.4 ± 0.3%). The highest mean absorbed doses of radiation were in the gallbladder wall (242.2 ± 105.2 μGy/MBq), upper large intestine (90.0 ± 15.8 μGy/MBq), small intestine

(79.5 ± 13.8 µGy/MBq), and liver (55.8 ± 6.1 µGy/MBq). The resultant

whole-body effective dose was 22.7 ± 1.3 µSv/MBq.

Conclusion: Our results suggest that a routine injection of 370 MBq of

^{18}F-THK-5351 would lead to an estimated effective dose of 8.4 mSv; hence,

^{18}F-THK-5351 shows similar radiation burdens to other commonly used clinical

tracers. Our findings in humans were compatible with recently published

preclinical dosimetry data extrapolated from mice.

Keywords: ^{18}F-THK-5351, Alzheimer's disease, tau, whole body biodistribution,

radiation dosimetry

Introduction

Alzheimer's disease (AD) is the most common type of dementia. The hallmark pathology of this disease involves the accumulation of beta-amyloid plaques and tau proteins (*1,2*). In addition, the spatial spreading of these biomarkers is indicative of the temporal progression of AD (*3,4*).

Fortunately, the rapid development of molecular imaging techniques and tracers has permitted the early detection and diagnosis of AD (*5*). One of the earliest successfully introduced tracers in clinical studies is Pittsburgh Compound-B, which binds to amyloid with low nanomolar affinity (*6*). Since then, more widely distributable tracers labeled with ^{18}F, including ^{18}F-flutemetamol, ^{18}F-florbetaben, and ^{18}F-florbetapir, have been approved for assessing the presence of amyloid plaques in clinical settings and have encouraged researchers to perform clinical trials aimed at developing novel therapeutic strategies (*7*).

However, beta-amyloid plaques initially develop in preclinical AD, and the amyloid burden, as imaged with positron emission tomography (PET), does not appear to correlate with the clinical symptoms of late mild cognitive impairment (MCI) and AD (*8-11*). On the other hand, tau aggregation, in the form of neurofibrillary tangles, which first appears in the mesial temporal region and then spreads to the neocortex, is associated with the clinical stage of AD (*11,12*). In this regard, the non-invasive imaging of tau could potentially facilitate the early diagnosis of AD, help differentiate it from other dementing disorders, and allow

researchers to evaluate the outcomes of tau immunization therapies (*13*).

Given their potential, researchers have been focused on developing radiotracers for imaging tau protein in the brain (*14-19*). Since tau aggregates are mainly located intracellularly and may co-exist with amyloid plaques, the success of *in vivo* human imaging relies on the ability of the radiotracer to cross the blood-brain barrier with high selectively for the target. Some of the proposed tau tracers have met the above criteria and are currently undergoing clinical assessments, including the THK analogs ^{18}F-THK-5105, ^{18}F-THK-5117 (*16*), ^{11}C-PBB3 (*17*), and ^{18}F-AV-1451 (formerly called ^{18}F-T807) (*19*). However, tracers like ^{18}F-THK-5117 showed relatively high nonspecific uptake in the subcortical white matter, which might hinder the visual interpretation of PET images. To reduce nonspecific tracer retention in the white matter, Harada and colleagues (*20*) developed a novel tau PET tracer, ^{18}F-THK-5351, by replacing a benzene ring of ^{18}F-THK-5117 with pyridine. The preliminary data for ^{18}F-THK-5351 showed faster kinetics, higher contrast, and lower retention in the subcortical white matter when compared to ^{18}F-THK-5117 (*20*). However, the internal radiation dosimetry data for ^{18}F-THK-5351 have not yet been published.

In the present study, we aimed to provide estimates of the radiation doses of the radiotracer ^{18}F-THK-5351 to the whole body and various organs in humans. To do this, we intravenously injected ^{18}F-THK-5351 into 12 healthy human volunteers and performed organ time-activity measurements with whole-body

PET images to define the tissue concentration of the injected radiotracer. Then, the absorbed doses were estimated, and the effective doses were calculated with the medical internal radiation dosimetry method using the OLINDA software (Vanderbilt University, Nashville, TN, USA) by modifying the standard reference phantoms with subject-specific masses.

Methods

Subjects

Twelve healthy control subjects were recruited for this study (age range, 34–54 years; 7 men, 5 women; Table 1). None of the subjects demonstrated any clinically significant abnormalities during their physical or neurological examinations. All subjects' laboratory investigation results were in the normal range. Safety data including vital signs, electrocardiograms, and laboratory parameters were collected before and at 5 h after injection for comparison. The study was approved by the Institutional Review Board at Chang Gung Memorial Hospital. Informed written consent was obtained from each subject after providing the subjects with a detailed explanation of the study. The trial was registered with clinicaltrials.gov (NCT02686216).

Preparation of ^{18}F-THK-5351

The radiotracer was synthesized using the methods of Harada et al. (*20*),

7

with slight modifications. Our modifications included using less precursor (1 mg

instead of 3 mg) and the addition of sodium ascorbate (0.5% w/v) in the mobile

phase of high-performance liquid chromatography purification to prevent

radiolysis of the product. In brief, ^{18}F-THK-5351 was prepared from its tosylate

precursor

(S)-2-(2-methylaminopyrid-5-yl)-6-[[2-(tetrahydro-2H-pyran-2-yloxy)-3-tosyloxy

]propoxy] quinoline (THK-5352) according to the previously described method

for synthesizing ^{18}F-THK-5105 and ^{18}F-THK-5117 (*16*). ^{18}F-THK-5351 was

purified using semipreparative high-performance liquid chromatography (column:

Inertsil ODS-4; GL Sciences, Inc.; mobile phase: 20 mM NaH_2PO_4/acetonitrile

[75:25], flow rate: 5.0 mL/min). ^{18}F-THK-5351 was obtained at a radiochemical

yield of 30 ± 4% (decay-corrected) with a radiochemical purity of >95% and

specific activity of 178.8 ± 32.1 TBq/mmol (n = 8). The radiotracer was

formulated in a saline solution containing ethanol (7%), sodium ascorbate (0.5%),

and polysorbate-80 (0.15%) for clinical evaluation.

Whole-body and brain PET imaging

Serial PET scans of the whole body were performed on a dedicated

PET/computed tomography (CT) scanner (Siemens Biograph mCT 16; Siemens

Medical Solutions). Low-dose CT scans for attenuation correction were acquired

with the following parameters: 40 mAs, 120 keV, 512 × 512 matrix, 5-mm slice

thickness, 201 slices, 30 mm/s increments, 0.5-s rotation time, and pitch of 0.8. The imaging field ranged from the head to the proximal thighs. The ^{18}F-THK-5351 radiotracer was injected through a venous line into the arm of 12 subjects with a mean administered activity of 377.8 ± 14.0 MBq. The scanning protocol included 1–2 min emission scans for four cycles at 10, 60, 120, and 240 min post-injection. Each cycle consisted of seven bed positions, thus the whole-body scanning time was 10 min per cycle. Additional dynamic brain scans were acquired between the whole-body scanning sessions, ranging from 0–10 min, 20–60 min, and 70–90 min post-injection. Subjects were allowed to leave the scanner before the third and fourth whole-body scans. Prior to the third and fourth emission imaging sessions, additional whole-body CT attenuation correction scans were performed. All data were decay corrected to the starting time of each individual scan. All PET images were corrected for photon attenuation, dead time, random events, and scatter. Images were reconstructed in the three-dimensional mode using a manufacturer-supplied reconstruction technique (ordered-subsets expectation maximization with 16 subsets and two iterations).

The uptake of ^{18}F-THK-5351 in the target organs was determined by calculating the standardized uptake value (SUV) according to the following formula:

$$\text{SUV} = \frac{\text{Decay corrected tissue activity (Bq/mL)}}{\text{Injected dose (Bq)/Body weight (g)}}, \qquad \text{Eq. 1}$$

The mean SUV values of the organs of interest determined at time t after injection, i.e., $\overline{SUV}_{organ}(t)$, were assessed in all subjects.

Dosimetry

Full organ segmentation was performed manually on CT and PET images for the entire body and each visualized organ (brain, salivary gland, thyroid, lung, liver, gallbladder, heart, kidneys, spleen, and bladder) using the PMOD image analysis software, version 3.2 (PMOD Technologies Ltd, Zurich, Switzerland). Bone marrow dosimetry was derived from CT-based volumes of interest that were placed over lumbar vertebrae 2–4. All volumes of interest were drawn subjectively around each organ by an experienced nuclear medicine physician (KJ). The mean SUV from each target was then converted to the percent injected dose (%ID) by using the known mass of an organ or its contents, as follows:

$$\%\text{ID (t)} = 100\% \times \overline{SUV}_{organ}(t) \times \frac{V_{organ}}{M_{body}}, \qquad \text{Eq. 2}$$

where *%ID(t)*, *V$_{organ}$*, and *M$_{body}$* are the percent injected dose measured at time t after injection, the volume of the organ (mL), and the mass (g) of the whole body, respectively. Time-activity curves for the organs were fit to a nonlinear regression model of exponential uptake and clearance using the OLINDA/EXM software. For organs without an exponential curve pattern, such as the gallbladder, the area under the curve was calculated from the available time-activity curve via the

trapezoidal rule method. For a conservative analysis, the activity after the last

time point was considered radioactivity decay. The residence times for the bowel

and bladder were calculated using the ICRP 30 GI model and dynamic bladder

model as incorporated in OLINDA, respectively. In the bladder model, the

maximum cumulated activity of the urinary bladder content was determined by

fitting the bladder time-activity curve with an exponential growth function. A

remainder term was computed for activity in the body that was not specifically

visualized in an organ (1 − all specific organs). Residence times were input into

the OLINDA/EXM software for each organ based on the adult model; we also

modified the standard reference phantoms with subject-specific masses to

compute the individual organ doses and effective dose equivalent (*21*). The

OLINDA/EXM software multiplies the residence time for each subject and organ

by the S value (mSv/MBq × h) to obtain the dose, as follows:

$$\text{Dose (mSv/MBq)} = \text{residence time (h)} \times \text{S value.} \qquad \text{Eq. 3}$$

S values are implemented within the OLINDA/EXM software.

Results

The ^{18}F-THK-5351 injection was found to be safe and tolerable, and no

immediate adverse events were observed in any of the 12 subjects. No significant

11

changes in the subjects' vital signs (heart rate, blood pressure, and respiratory rate); electrocardiograms; and laboratory parameters, including serum chemistry and hematology, were noted after ^{18}F-THK-5351 injection compared to before injection. The whole-body images from a representative subject are presented in Fig. 1. Uptake of the radiotracer in the lung, kidney, and blood-containing organs occurred within 10 min after injection, followed by rapid clearance. Prominent liver and gallbladder uptake occurred at 60 min after injection, followed by a gradual decrease over the remaining study duration (Fig. 1). The bladder and bowel showed substantial uptake from 10 min toward the end owing to urine accumulation and radioactivity elimination through the gastrointestinal tract.

The time-activity curves of the decay-corrected %ID of each organ for all 12 subjects are shown in Fig. 2 and the specific values are listed in Supplemental Table 1. The time-activity curves showed high initial uptake of the radiotracer in the liver and lung, with values of 11.4 ± 2.0 and 5.7 ± 2.1 %ID, respectively. The organs with a fast wash-in and -out were the lungs, kidneys, heart, and thyroid. In contrast, the uptake and washout in the brain, bone marrow, and liver were gradual. The radiotracer uptake in the brain was 1.0 ± 0.2 %ID at 10 min after tracer injection. The maximum urinary bladder accumulated radioactivity was calculated as 4.9 ± 3.3 %ID with a biologic half-life of 1.1 ± 0.6 h (exponential growth curve fitting result from the biodistribution data). The residence times or average number of disintegrations were then calculated by using the area under

12

the fitting curves in the source organs (see Supplemental Table 2). Table 2 presents the dosimetry data including the effective dose equivalents for various organs in the 12 subjects. The mean effective dose for the 4.8-h bladder-voiding model was 22.7 ± 1.3 μSv/MBq.

Dynamic brain images at 0, 10, 50, 120, and 240 min post-injection are shown in Fig. 3. The early-phase brain image was averaged from the 0–10-min dynamic brain scan, while the other brain images were reconstructed from the whole-body scans. These serial, 10-min brain scans of healthy subjects demonstrate that images of adequate quality can be acquired with a 370-MBq (10-mCi) injection. The early phase (0–10 min) brain image shows a perfusion-like distribution of radiotracer with cortical and subcortical uptake, as expected. As for the brain, the SUVs at 10 min post-injection were the highest in the striatum (1.95 ± 0.51), followed by the medial temporal (1.42 ± 0.33), frontal (1.23 ± 0.35), and parietal (1.14 ± 0.30) regions and cerebellum (1.13 ± 0.30). Ten minutes after injection, the radiotracer washed out quickly from most of the brain regions except the basal ganglia, thalamus, medial temporal region, and midbrain areas, which showed substantial retention of the radioactivity. In the late phase (after 50 min), no definite retention or uptake of radioactivity was noted in the brain except for blood pool activity in the internal carotid artery.

Discussion

13

To the best of our knowledge, this study is the first human clinical trial to directly evaluate the biodistribution and whole-body radiation dosimetry of ^{18}F-THK-5351. Here, we revealed that the ^{18}F-THK-5351 biodistribution was dominated by activity in the hepatobiliary system, with little renal clearance. The highest doses were recorded in the gallbladder (242.2 ± 105.2 µGy/MBq), upper large intestine (90.0 ± 15.8 µGy/MBq), small intestine (79.5 ± 13.8 µGy/MBq), and liver (55.8 ± 6.1 µGy/MBq). The dosimetry data showed that to avoid exceeding a 50-mGy dose to the critical organ, i.e., the liver, the maximum injected dose that can be used in a ^{18}F-THK-5351 study is 896 MBq (24.2 mCi). The estimated effective dose was 22.7 µSv/MBq, which is in the same range (20–30 µSv/MBq) as that for other ^{18}F-labeled radiopharmaceuticals. For a routine injection dose of 175 MBq (5 mCi) or a higher dose of 370 MBq for research purposes, the whole-body doses are estimated to be 4.2 and 8.3 mSv, respectively, which are well below the whole-body dose limit of 30 mSv (single dose) specified by the Food and Drug Administration for research subjects (22).

When comparing our human data to data derived by harvesting organs from mice, the initial distribution of the radioactivity seemed similar, showing dominant hepatobiliary uptake (20). However, the clearance of the radiotracer from the liver and lung was much faster in mice than it was in humans, and the absorbed doses calculated with the extrapolation method for the liver and lung were underestimated by factors of 5 and 2, respectively, compared to our clinical

14

values (9.4 vs. 55.8 μGy/MBq for the liver and 8.0 vs. 17.4 μGy/MBq for the lung). This discrepancy is generally related to interspecies differences in metabolism. Although the mouse-derived measurement was roughly comparable to the human-derived dose (18.4 vs. 22.7 μSv/MBq), considerable differences in the critical organ dose estimates and pharmacokinetics were found for this novel radiotracer. In this regards, human whole-body imaging for investigating the biodistribution of ^{18}F-THK-5351 instead of animal data alone is desirable for making initial evaluations prior to the wide clinical application of this tracer (*23*).

In the present study, high variability (variation coefficient >20%) in the measured residence time and estimated absorbed doses were found in the gallbladder and urinary bladder wall. Since we did not limit the subjects' intake of food and water before and during the study period, this high variability was most likely related to differences in the functional clearance rate among the subjects.

As observed in our dynamic brain images, substantial radioactivity retention occurred in the basal ganglia. Although tau pathology has been reported in the basal ganglia of individuals with AD (*24*), data on the striatal uptake of ^{18}F-THK-5351 from *in vitro* autoradiography and binding assay studies are limited and inconclusive (*20,25*). This substantial radioactivity retention in the basal ganglia may also be related to off-target binding, as suggested by studies on other tau-seeking radiotracers like AV-1451 (*26*). However, despite the potential for off-target binding in subcortical structures, no significant retention of

15

^{18}F-THK-5351 was observed in the choroid plexus or venous sinus as compared to ^{18}F-AV-1451, which is in line with the findings of a previous report (*20*).

One limitation of our biodistribution study is the lack of time points at later time frames. This type of study is difficult to perform since our Radiation Safety Committee and Institutional Review Board asked us to minimize the radiation exposure for research purposes, thus we omitted the time point at 4 h post-injection to reduce the need for an additional attenuation CT dose. For organs that do not fit the exponential decay curve, the remaining radioactivity in each organ was conservatively assumed to be removed through physical decay only after the last measured time point. In addition, since the whole-body images were collected using multiple bed positions, the exact acquisition time points for individual organs will likely not be the same as those estimated in our study. These subtle timing differences may affect the time-activity curve of each organ and the final estimates of the radiation absorbed doses. Another limitation is that the mean age of the subjects in this biodistribution study was relatively low as compared to that of the general dementia target group. Thus, the possibility of heterogeneous biodistributions at different ages cannot be excluded.

Conclusion

The present whole-body biodistribution study with ^{18}F-THK-5351 demonstrated that a routine injection of 370 MBq of ^{18}F-THK-5351 would lead to

an estimated effective dose of 8.4 mSv. Importantly, ^{18}F-THK-5351 shows similar radiation burdens to other widely used clinical tracers. The results found here in humans were compatible with recently published preclinical dosimetry data extrapolated from mice, although some differences in the individual organ dose estimates and pharmacokinetics were noted for the lung and liver. The radiation risk profile we identified suggests that a subject could safely receive multiple injections of ^{18}F-THK-5351 or injections of ^{18}F-THK-5351 in conjunction with other brain radiotracers in a single year.

Disclosure

Acknowledgments

References

1. Hardy J, Selkoe DJ. The amyloid hypothesis of Alzheimer's disease: progress and problems on the road to therapeutics. *Science.* 2002;297:353–356.

2. Alonso AC, Grundke-Iqbal I, Iqbal K. Alzheimer's disease hyperphosphorylated tau sequesters normal tau into tangles of filaments and disassembles microtubules. *Nat Med.* 1996;2:783–787.

3. Arnold SE, Hyman BT, Flory J, Damasio AR, Van Hoesen GW. The topographical and neuroanatomical distribution of neurofibrillary tangles and neuritic plaques in the cerebral cortex of patients with Alzheimer's disease. *Cereb Cortex.* 1991;1:103–116.

4. Braak H, Braak E. Staging of Alzheimer's disease-related neurofibrillary changes. *Neurobiol Aging.* 1995;16:271–284.

5. McKhann GM, Knopman DS, Chertkow H, et al. The diagnosis of dementia due to Alzheimer's disease: recommendations from the National Institute on Aging-Alzheimer's Association workgroups on diagnostic guidelines for Alzheimer's disease. *Alzheimers Dement.* 2011;7:263–269.

6. Klunk WE, Engler H, Nordberg A, et al. Imaging brain amyloid in Alzheimer's disease with Pittsburgh Compound-B. *Ann Neurol.* 2004;55:306–319.

7. Sevigny J, Chiao P, Bussière T, et al. The antibody aducanumab reduces Aβ

plaques in Alzheimer's disease. *Nature*. 2016;537:50–56.

8. Lin K-J, Hsiao T, Hsu J-L, et al. Imaging characteristic of dual-phase 18F-florbetapir (AV-45/Amyvid) PET for the concomitant detection of perfusion deficits and beta-amyloid deposition in Alzheimer's disease and mild cognitive impairment. *Eur J Nucl Med Mol Imaging*. 2016;43:1304–1314.

9. Jack CR, Wiste HJ, Lesnick TG, et al. Brain β-amyloid load approaches a plateau. *Neurology*. 2013;80:890–896.

10. Huang KL, Lin KJ, Hsiao IT, et al. Regional amyloid deposition in amnestic mild cognitive impairment and Alzheimer's disease evaluated by [18F]AV-45 positron emission tomography in Chinese population. *PLoS One*. 2013;8:e58974.

11. Arriagada PV, Growdon JH, Hedley-Whyte ET, Hyman BT. Neurofibrillary tangles but not senile plaques parallel duration and severity of Alzheimer's disease. *Neurology*. 1992;42:631–639.

12. Bierer LM, Hof PR, Purohit DP, et al. Neocortical neurofibrillary tangles correlate with dementia severity in Alzheimer's disease. *Arch Neurol*. 1995;52:81–88.

13. Wang L, Benzinger TL, Su Y, et al. Evaluation of tau imaging in staging Alzheimer disease and revealing interactions between β-amyloid and tauopathy. *JAMA Neurol*. 2016;73:1070–1077.

14. Small GW, Kepe V, Huang SC, et al. P2-206 In vivo brain imaging of tau aggregation in frontal temporal dementia using [F-18]FDDNP positron emission tomography. *Neurobiol Aging.* 2004;25:S288–S289.

15. Shao X, Carpenter GM, Desmond TJ, et al. Evaluation of [11C]N-methyl lansoprazole as a radiopharmaceutical for PET imaging of tau neurofibrillary tangles. *ACS Med Chem Lett.* 2012;3:936–941.

16. Okamura N, Furumoto S, Harada R, et al. Novel 18F-labeled arylquinoline derivatives for noninvasive imaging of tau pathology in Alzheimer disease. *J Nucl Med.* 2013;54:1420–1427.

17. Hashimoto H, Kawamura K, Igarashi N, et al. Radiosynthesis, photoisomerization, biodistribution, and metabolite analysis of 11C-PBB3 as a clinically useful PET probe for imaging of tau pathology. *J Nucl Med.* 2014;55:1532–1538.

18. Zimmer ER, Leuzy A, Gauthier S, Rosa-Neto P. Developments in tau PET imaging. *Can J Neurol Sci.* 2014;41:547–553.

19. Chien DT, Bahri S, Szardenings AK, et al. Early clinical PET imaging results with the novel PHF-tau radioligand [F-18]-T807. *J Alzheimers Dis.* 2013;34:457–468.

20. Harada R, Okamura N, Furumoto S, et al. 18F-THK5351: a novel PET radiotracer for imaging neurofibrillary pathology in Alzheimer disease. *J Nucl Med.* 2016;57:208–214.

21. Stabin MG, Sparks RB, Crowe E. OLINDA/EXM: the second-generation personal computer software for internal dose assessment in nuclear medicine. *J Nucl Med.* 2005;46:1023–1027.

22. Guidance for industry and researchers: The Radioactive Drug Research Committee—human research without an investigational new drug application. U.S. Food and Drug Administration website. http://www.fda.gov/downloads/drugs/guidancecomplianceregulatoryinformation/guidances/ucm163892.pdf. Published August 2010. Accessed March 3, 2015.

23. Sakata M, Oda K, Toyohara J, Ishii K, Nariai T, Ishiwata K. Direct comparison of radiation dosimetry of six PET tracers using human whole-body imaging and murine biodistribution studies. *Ann Nucl Med.* 2013;27:285–296.

24. Braak H, Braak E. Alzheimer's disease: striatal amyloid deposits and neurofibrillary changes. *J Neuropathol Exp Neurol.* 1990;49:215–224.

25. Lemoine L, Saint-Aubert L, Marutle A, et al. Visualization of regional tau deposits using (3)H-THK5117 in Alzheimer brain tissue. *Acta Neuropathol Commun.* 2015;3:40.

26. Lowe VJ, Curran G, Fang P, et al. An autoradiographic evaluation of AV-1451 Tau PET in dementia. *Acta Neuropathol Commun.* 2016;4:58.
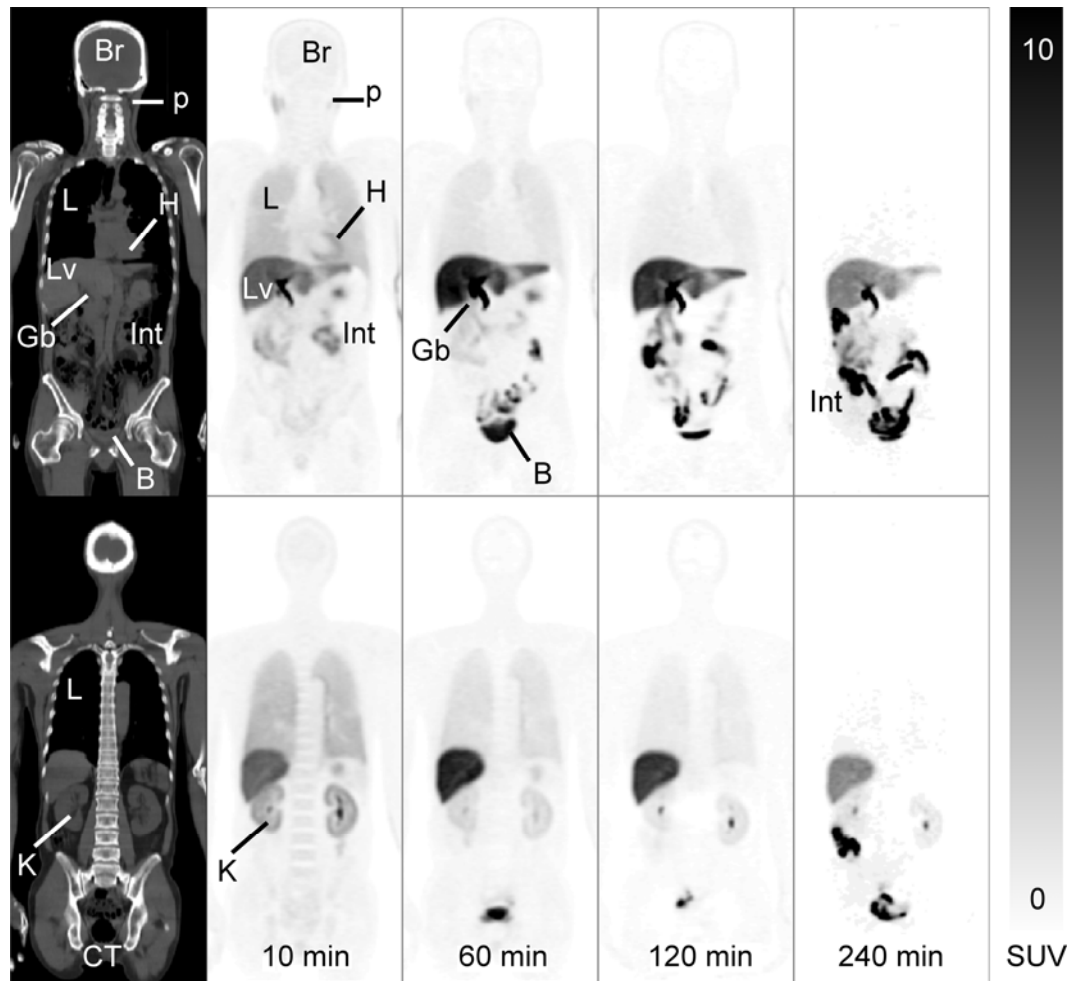
Figures

FIGURE 1. Coronal sequential whole-body positron emission tomography images (75-mm thick) at 10, 60, 120, and 240 min after the injection of ^{18}F-THK-5351 and the corresponding computed tomography (CT) images in a healthy 53-year-old woman. Images show the standardized uptake value (SUV) according to the scale on the right. B: bladder; Br: brain; Gb: gallbladder; H: heart; Int: intestine; K: kidney; L: lung; Lv: liver; p: parotid gland.

22
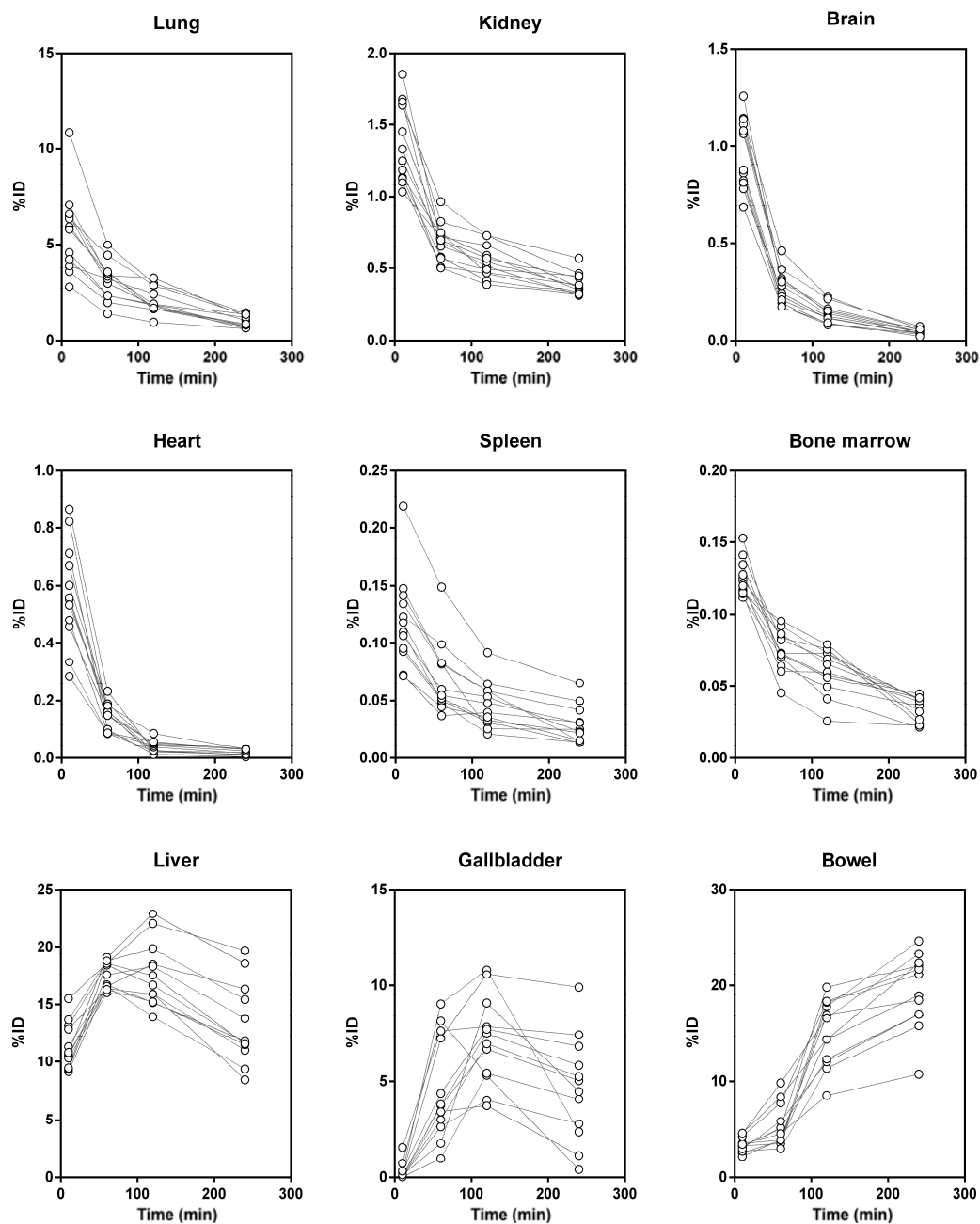
FIGURE 2. The fractional activity in various organs with respect to the total body activity (percent injected dose, %ID) for the 12 subjects.

FIGURE 3. Brain images from a 47-year-old woman. The first column shows her structural magnetic resonance images (MRI). The remaining columns display her brain positron emission tomography images acquired in the early (0–10 min), mid (10–20 min), and late (after 50 min) phases after ^{18}F-THK-5351 injection. The color scale represents the standardized uptake value (SUV).

Tables

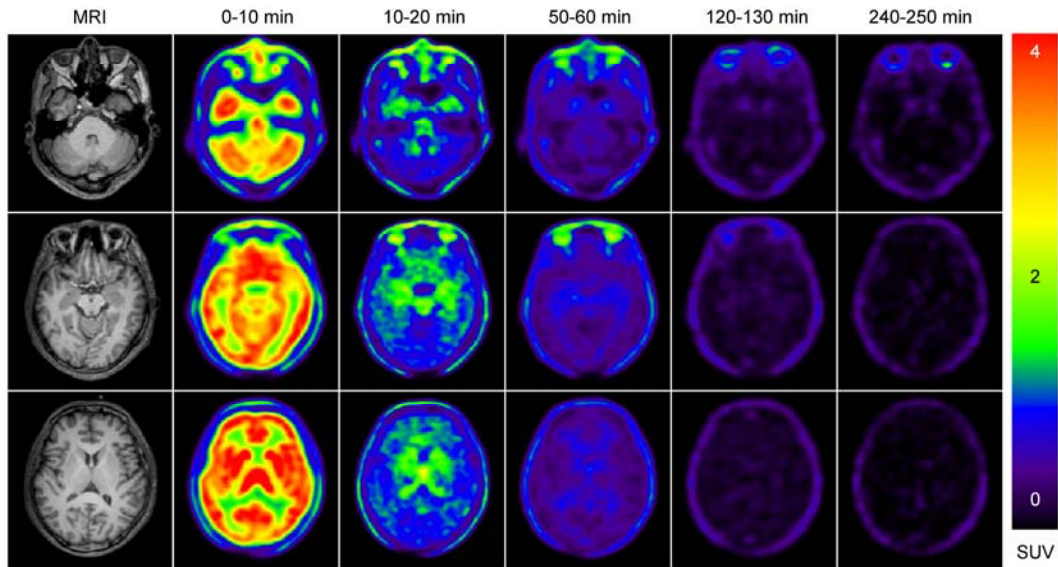TABLE 1. Demographics of the study subjects.

Subject no.	Sex	Age (years)	Mass (kg)	ID (MBq)
1	M	52	53	389
2	M	49	54	377
3	F	47	53	397
4	F	45	53	340
5	M	47	59	388
6	F	48	70	379
7	M	46	65	370
8	F	39	65	376
9	M	38	97	382
10	M	38	76	383
11	M	34	100	374
12	M	54	73	379
Mean $\pm$ SD		44.8 $\pm$ 6.2	68.2 $\pm$ 16.3	377.8 $\pm$ 14.0

ID: injection dose; M: male; F: female; SD: standard deviation.

TABLE 2. Dosimetry for ^{18}F-THK-5351 from 12 subjects.

Parameter/Organ	μGy/MBq (mean)	mrad/mCi (mean)	CV (%)
Adrenals	15.9	589.	5.0
Brain	2.9	10.8	10.7
Breasts	8.6	31.7	11.7
Gallbladder	242.2	896.3	43.4
LLI	34.6	128.2	14.8
Small Intestine	79.5	294.0	17.4
Stomach	18.4	68.2	6.4
ULI	90.0	333.0	17.5
Heart	10.3	38.2	6.4
Kidneys	20.9	77.5	8.4
Liver	55.8	206.6	10.9
Lungs	17.4	64.2	19.0
Muscle	11.4	42.0	9.3
Ovaries (n = 4)	21.7	80.1	11.1
Pancreas	17.9	66.4	5.2
Bone Marrow	11.7	43.1	8.2
Osteogenic Cells	15.4	56.8	14.2
Skin	8.0	29.6	12.7
Spleen	8.8	32.6	5.8
Testes (n = 8)	8.8	32.5	13.0
Thymus	10.0	36.9	11.3
Thyroid	5.7	21.1	10.5
Urinary Bladder	42.4	156.8	29.2
Uterus	21.0	77.5	14.8
Total Body	14.5	53.5	18.9
Effective dose equivalent	41.6*	153.9[†]	16.4
Effective dose	22.7*	84.0[†]	5.8

*μSv/MBq; †mrem/mCi.

Urinary bladder clearance model with 4.8-h voiding intervals.

CV: percentage coefficient of variation calculated as the (standard deviation/mean) × 100%; LLI: lower large intestine; ULI: upper large intestine.

SUPPLEMENTAL TABLE 1. Biodistribution of ^{18}F-THK-5351 in each organ at various time points after intravenous injection.

Organ	10 min	60 min	120 min	240 min
Brain	0.97 ± 0.18	0.27 ± 0.08	0.14 ± 0.05	0.05 ± 0.02
Lung	5.67 ± 2.14	3.11 ± 1.00	2.07 ± 0.65	1.02 ± 0.31
Myocardium	0.57 ± 0.18	0.14 ± 0.05	0.04 ± 0.02	0.02 ± 0.01
Liver	11.40 ± 1.97	17.47 ± 1.16	17.67 ± 2.81	13.26 ± 3.54
Gallbladder	0.29 ± 0.44	4.65 ± 2.66	7.13 ± 2.29	4.62 ± 2.71
Stomach	0.71 ± 0.18	0.51 ± 0.13	0.35 ± 0.15	0.19 ± 0.12
Spleen	0.12 ± 0.04	0.07 ± 0.03	0.05 ± 0.02	0.03 ± 0.02
Kidneys	1.37 ± 0.28	0.68 ± 0.13	0.55 ± 0.11	0.39 ± 0.08
Intestine	3.37 ± 0.77	5.39 ± 2.18	15.03 ± 3.45	19.41 ± 3.91
Bone Marrow	0.12 ± 0.01	0.07 ± 0.01	0.06 ± 0.02	0.03 ± 0.01
Urinary Bladder	0.37 ± 0.28	2.47 ± 1.01	1.28 ± 1.60	1.81 ± 2.43
Uterus (n = 4)	0.33 ± 0.29	0.15 ± 0.13	0.10 ± 0.07	0.04 ± 0.01

Bone marrow data are scaled from lumbar vertebrae.

Values are the percent injected dose/organ (%ID) from 12 subjects except where noted.

SUPPLEMENTAL TABLE 2. Average number of disintegrations in the source organs.

Source Organ	MBq-h/MBq (mean ± SD)	CV (%)
Liver	3.88E-01 ± 5.27E-02	13.6
Gallbladder Contents	1.39E-01 ± 6.76E-02	48.5
Bone Marrow	1.51E-03 ± 3.03E-04	20.1
Brain	6.46E-03 ± 1.56E-03	24.2
Lungs	6.43E-02 ± 1.95E-02	30.2
Small Intestine	3.09E-01 ± 6.23E-02	20.2
Upper Large Intestine	1.69E-01 ± 3.40E-02	20.1
Lower Large Intestine	3.10E-02 ± 6.24E-03	20.2
Stomach	1.06E-02 ± 4.04E-03	38.1
Kidneys	1.60E-02 ± 3.18E-03	19.9
Spleen	1.30E-03 ± 4.94E-04	38.0
Heart	3.54E-03 ± 9.25E-04	26.1
Thyroid	8.66E-05 ± 5.49E-05	63.5
Testes (n = 8)	6.09E-04 ± 5.28E-05	8.7
Ovaries (n = 4)	8.55E-05 ± 2.36E-05	27.6
Uterus	2.54E-03 ± 2.15E-03	84.5
Remainder	1.66E+00 ± 1.03E-01	6.2
Urinary Bladder	6.36E-02 ± 2.86E-02	45.0

SD: standard deviation; CV: percentage coefficient of variation calculated as the (standard deviation/mean) $\times$ 100%.

Data are from 12 subjects unless otherwise noted.

Bone marrow data are scaled from lumbar vertebrae.

Urinary bladder clearance model with 4.8-h voiding intervals.